ADVANCED FUNCTIONAL MATERIALS
www.afm-journal.de

Dental Resin Monomer Enables Unique NbO_2/Carbon Lithium-Ion Battery Negative Electrode with Exceptional Performance

Qing Ji, Xiangwen Gao, Qiuju Zhang, Liyu Jin, Da Wang, Yonggao Xia, Shanshan Yin, Senlin Xia, Nuri Hohn, Xiuxia Zuo, Xiaoyan Wang, Shuang Xie, Zhuijun Xu, Liujia Ma, Liang Chen, George Z. Chen, Jin Zhu,* Binjie Hu,* Peter Müller-Buschbaum, Peter G. Bruce, and Ya-Jun Cheng**

Niobium dioxide (NbO_2) features a high theoretical capacity and an outstanding electron conductivity, which makes it a promising alternative to the commercial graphite negative electrode. However, studies on NbO_2 based lithium-ion battery negative electrodes have been rarely reported. In the present work, NbO_2 nanoparticles homogeneously embedded in a carbon matrix are synthesized through calcination using a dental resin monomer (bisphenol A glycidyl dimethacrylate, Bis-GMA) as the solvent and a carbon source and niobium ethoxide (NbETO) as the precursor. It is revealed that a low Bis-GMA/NbETO mass ratio (from 1:1 to 1:2) enables the conversion of Nb (V) to Nb (IV) due to increased porosity induced by an alcoholysis reaction between the NbETO and Bis-GMA. The as-prepared NbO_2/carbon nanohybrid delivers a reversible capacity of 225 mAh g^{-1} after 500 cycles at a 1 C rate with a Coulombic efficiency of more than 99.4% in the cycles. Various experimental and theoretical approaches including solid state nuclear magnetic resonance, ex situ X-ray diffraction, differential electrochemical mass spectrometry, and density functional theory are utilized to understand the fundamental lithiation/delithiation mechanisms of the NbO_2/carbon nanohybrid. The results suggest that the NbO_2/carbon nanohybrid bearing high capacity, long cycle life, and low gas evolution is promising for lithium storage applications.

1. Introduction

Intercalation type lithium-ion battery negative electrodes hold a great promise to be an alternative to the commercial graphite negative electrode, primarily because of their proper voltage profile and outstanding operation safety.[1] Compared to the typical intercalation negative electrodes such as TiO_2, $Li_4Ti_5O_{12}$, and Nb_2O_5, in particular niobium dioxide (NbO_2) bears a few distinct advantages.[2] It features a higher theoretical capacity (429 mAh g^{-1}), a lower lithiation/delithiation potential (around 1.3 V/1.4 V), and a superior electron conductivity (2 mag higher than that of Nb_2O_5 and 9 mag higher than that of $Li_4Ti_5O_{12}$).[3] Thus, exploring the capability of NbO_2 based lithium-ion battery negative electrodes is of fundamental importance as well as of practical relevance.

Despite the clear intrinsic advantages of NbO_2, only a very few studies about NbO_2 have been reported so far.[3,4] Anyhow, it will be essential to develop a facile scalable synthesis method, to investigate the

Q. Ji, Dr. Q. Zhang, Prof. Y. Xia, Dr. X. Zuo, Dr. X. Wang, S. Xie, Z. Xu, L. Ma, Prof. L. Chen, Prof. J. Zhu, Prof. Y.-J. Cheng
Ningbo Institute of Materials Technology and Engineering
Chinese Academy of Sciences
1219 Zhongguan West Road, Zhenhai District
Ningbo 315201, P. R. China
E-mail: xiayg@nimte.ac.cn; jzhu@nimte.ac.cn; chengyj@nimte.ac.cn

The ORCID identification number(s) for the author(s) of this article can be found under https://doi.org/10.1002/adfm.201904961.

DOI: 10.1002/adfm.201904961

Q. Ji, Prof. G. Z. Chen, Dr. B. Hu
Department of Chemical and Environment Engineering
Faculty of Science and Engineering
The University of Nottingham Ningbo China
199 Taikang East Road, Ningbo 315100, P. R. China
E-mail: Binjie.hu@nottingham.edu.cn

Dr. X. Gao, Dr. L. Jin, Dr. D. Wang, Prof. P. G. Bruce, Prof. Y.-J. Cheng
Department of Materials
University of Oxford
Parks Rd, Oxford OX1 3PH, UK

Prof. Y. Xia
Center of Materials Science and Optoelectronics Engineering
University of Chinese Academy of Sciences
19A Yuquan Rd, Shijingshan District, Beijing 100049, P. R. China

intercalation behavior and to reveal the fundamental mechanisms of NbO_2 based lithium-ion battery negative electrodes. A size reduction to the nanoscale range is identified of being crucial to demonstrate electrochemical activity toward lithium intercalation, where micrometer and sub-micrometer-sized particles only possess very limited actual capacities.[2e] The deposition of nanosized Nb_2O_5 particles onto a carbon foam followed by high-temperature annealing in a reducing atmosphere proved to be an effective way to synthesize NbO_2 nanoparticles bearing a reasonable electrochemical performance in lithium microbatteries.[4b] Nevertheless, the limited amount of NbO_2 nanoparticles within the carbon foam resulted in a low total energy output, which made it only suitable for microbatteries. Hydrothermal reaction was applied to synthesize NbO_2/carbon core shell nanocomposites, which showed a good electrochemical performance in super capacitors.[4a] However, an application as lithium-ion battery negative electrode was not addressed. Besides, the suggested synthetic method will be difficult to scale up, which renders this approach from the literature to be nonfeasible for practical applications.

In our previous work, a new concept was developed to synthesize intercalation negative electrode in a facile scalable way. TiO_2/C and $Li_4Ti_5O_{12}$/C nanohybrid particles with super-small-sized TiO_2 or $Li_4Ti_5O_{12}$ nanoparticles were in situ formed and homogeneously embedded in a carbon matrix.[5] The dental resin monomers of bisphenol A glycidyl dimethacrylate (Bis-GMA) and triethylene glycol dimethacrylate were used as solvent and carbon source, coupled with photo polymerization. Liquid metal oxide precursors such as titanium tetra isopropoxide were dissolved in the resin monomer solution, which were incorporated into the cross-link polymer network upon polymerization. Due to a limited melting process of the cross-linking network during calcination, particle growth and agglomeration of TiO_2 were significantly inhibited, leading to in situ formation of super-small-sized TiO_2 nanoparticles (less than 10 nm) which are homogeneously embedded inside the micrometer-sized in situ formed carbon matrix. The composition of super-small TiO_2 nanoparticles and carbon matrix exhibited a unique electrochemical performance as lithium-ion battery negative electrodes. Potential drawbacks related to nanostructured materials such as a low tap density, while side reactions induced by high chemical reactivity were effectively suppressed by the nanohybrid structure feature.[5b,6]

Based on the pioneering work of our group, here, we report a new facile scalable way to synthesize NbO_2/carbon nanohybrids with super-small-sized NbO_2 nanoparticles homogeneously embedded in the carbon matrix. The niobium oxide precursor (niobium (V) ethoxide, NbETO) is dissolved in a resin monomer solution of bisphenol A glycerolate methacrylate (B resin), which is cured via thermally induced polymerization. The Nb (V) species is reduced to Nb (IV) to form NbO_2 nanoparticles within the carbon matrix during a one-step heat treatment at 900 °C in argon/hydrogen atmosphere. Comprehensive studies are performed to understand the formation mechanisms of the NbO_2 nanoparticles, the intercalation behavior, and the electrochemical mechanism when being used as lithium-ion battery negative electrodes.

2. Results and Discussion

2.1. Synthesis and Structure Characterization of NbO_2/Carbon Nanohybrids

Figure 1a illustrates the synthetic process of the NbO_2/carbon nanohybrids. NbETO is first dissolved in Bis-GMA to obtain a clear mixture of the resin and the niobium oxide precursor. Niobium species are incorporated into the Bis-GMA cross-linking network via an alcoholysis reaction between NbETO and hydroxyl groups. During calcination, NbO_2 nanoparticles are in situ generated and uniformly dispersed in the carbon matrix. The formation of the NbO_2 nanoparticles is confirmed by the X-ray diffraction (XRD) analysis (Figure 1b). Bragg peaks at 26.0°, 35.2°, 37.1°, 40.0°, 52.1°, and 53.5° indicate the existence of a pure tetragonal phase of NbO_2 (JCPDS No.43-1043). Raman spectra (Figure 1c) are used to further characterize the composition of the NbO_2/carbon nanohybrids. Typical peaks of disordered carbon (D-band) and graphitic carbon (G-band) are observed at 1360 and 1599 cm^{-1}.[7] Besides, small peaks are seen at 170, 333, and 405 cm^{-1}, referring to the fingerprint bands of NbO_2.[8] Moreover, thermo-gravimetric analysis (TGA) measurements of the NbO_2/carbon samples (Figure 1d) reveal a mass loss of 15.6%. It is noted that the TGA curves exhibit a small mass increase between 200 and 500 °C, which is assigned to the oxidation from NbO_2 to Nb_2O_5. By assuming that NbO_2 is fully converted to Nb_2O_5, from the TGA measurement, the actual NbO_2 mass content is calculated to be 79%. In addition, surface valence states of the NbO_2/carbon nanohybrids are investigated by X-ray photoelectron spectroscopy (XPS). The XPS survey spectra (Figure S1a, Supporting Information) confirm the existence of carbon, oxygen, and niobium. However, according to the high-resolution Nb-3d XPS spectra (Figure S1b, Supporting Information) only Nb^{5+} is detected for the samples, where the bonding energy peaks are located at 207 and 210 eV, respectively. Considering that the XPS technique is

S. Yin, Dr. S. Xia, Dr. N. Hohn, Prof. P. Müller-Buschbaum
Physik-Department
Lehrstuhl für Funktionelle Materialien
Technische Universität München
James-Franck-Str. 1, Garching 85748, Germany
Dr. X. Wang, S. Xie, Z. Xu
University of Chinese Academy of Sciences
19A Yuquan Rd, Shijingshan District, Beijing 100049, P. R. China
L. Ma
State Key Laboratory of Separation Membranes and Membrane Processes
Tianjin Polytechnic University
Tianjin 300387, P. R. China
Prof. G. Z. Chen
University of Nottingham
University Park, Nottingham NG7 2RD, UK
Prof. P. Müller-Buschbaum
Heinz Maier-Leibnitz Zentrum (MLZ)
Technische Universität München
Lichtenbergstr. 1, Garching 85748, Germany
Prof. P. G. Bruce
The Henry Royce Institute
Parks Road, Oxford OX1 3PH, UK
Prof. P. G. Bruce
The Faraday Institution
Quad One, Becquerel Avenue, Harwell Campus, Didcot OX11 0RA, UK

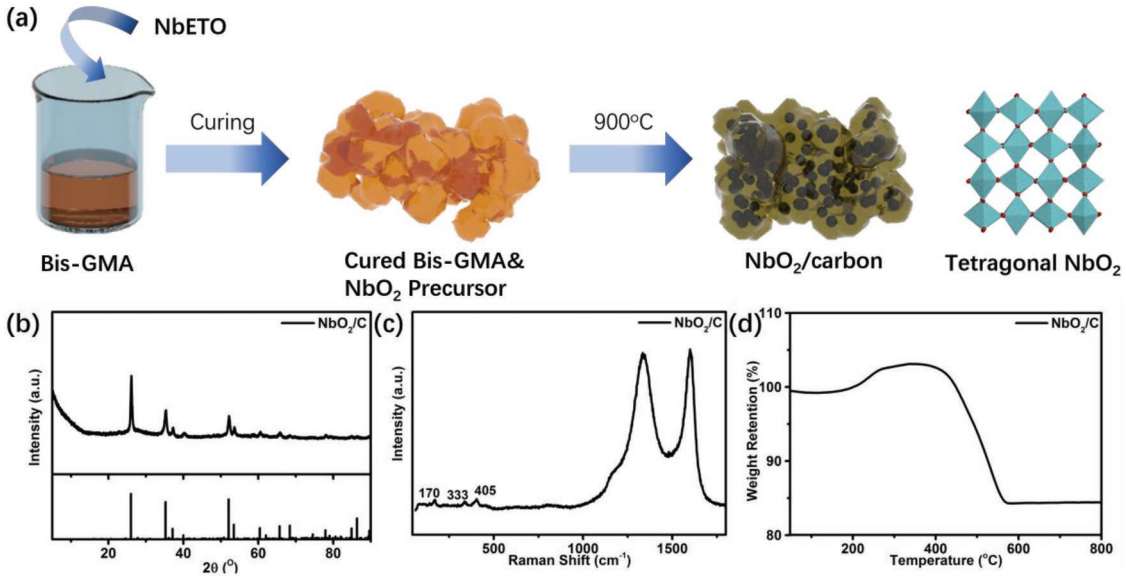

Figure 1. a) Schematic representation of the synthetic process, b) XRD data and expected peak positions, c) Raman spectra, and d) thermogravimetric profiles of NbO_2/carbon nanohybrids.

mainly sensitive to the surface element species, it is reasonable to conclude that the surface of the NbO_2/carbon nanohybrids is likely to be oxidized to Nb_2O_5.[4b,9] It is worth noting that the extent of the surface oxidation seems quite limited as the Nb_2O_5 species are barely detected with XRD in the NbO_2/carbon samples (Figure 1b).

Morphologies and microstructures of the NbO_2/carbon nanohybrids are investigated with scanning electron microscopy (SEM) and transmission electron microscopy (TEM). **Figure 2**a presents a rough surface built by loosely packed particles, which are regarded as individual NbO_2/carbon nanohybrid particles. The inset of the SEM images shows a size distribution of 5–10 µm for the micrometer-sized aggregated particles. The particle size distribution profiles (Figure S2, Supporting Information) reveal that the individual nanohybrids having sizes in the range between 300 and 600 nm dominate the samples. Due to the presence of a nanohybrid structure, the tap density (1.79 ± 0.03 g cm^3) is higher than in conventional nanostructured materials.[10] TEM images (Figure 2b) depict that the NbO_2 nanoparticles with a size of 20–30 nm are well embedded in the carbon matrix. High-resolution transmission electron microscopy (HRTEM) images (Figure 2c) display a set of fringes with a spacing of 0.34 nm, which refers to the (400) planes of the tetragonal NbO_2 phase. Selected area electron diffraction (SAED) patterns (Figure 2d) also confirm the existence of the (400), (222), and (262) planes of the tetragonal NbO_2 phase. In addition, scanning transmission electron microscopy (STEM) (Figure S3, Supporting Information) confirms the homogenous embedding of the NbO_2 nanoparticles within the carbon matrix.

The good control over the particle size and dispersion originates from the particular structure feature of the Bis-GMA resin

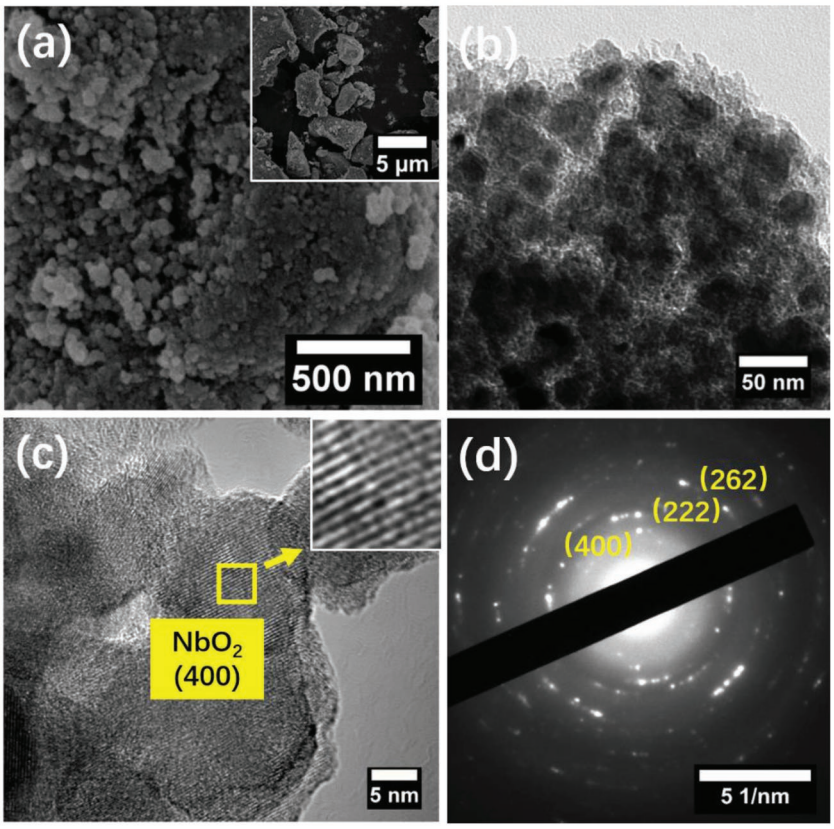

Figure 2. a) SEM, b) TEM, c) HRTEM, and d) SAED measurements of the NbO_2/carbon nanohybrids.

and the strong interaction between the niobium ethoxide and the Bis-GMA monomer. Firstly, the niobium species are homogeneously incorporated into the Bis-GMA cross-linking network at a molecular level with strong coordination bonding via an alcoholysis process. Secondly, the thermosetting poly (Bis-GMA) cross-linking network undergoes a very limited melting process during the carbonization at high temperatures. As a result, the nucleation, growth, and agglomeration of the NbO_2 particles are significantly inhibited. Thus, a homogenous distribution of the NbO_2 nanoparticles in the carbon matrix is achieved.

It is found that the mass ratio of Bis-GMA/NbETO plays an important role in the formation of the NbO_2 phase during the calcination process. Figure S4a in the Supporting Information shows that the samples with a Bis-GMA/NbETO mass ratio of 4:1, 2:1, and 1:1 present a hexagonal Nb_2O_5 phase (JCPDS No. 32-0710) after calcination at identical conditions. While with a mass ratio of 1:1.5, both hexagonal Nb_2O_5 and tetragonal NbO_2 phases are observed with XRD. This observation suggests that the NbO_2 phase is only formed with a low Bis-GMA/NbETO mass ratio, leading to a low carbon content in the NbO_2/carbon nanohybrids. In addition, according to Figure S4b in the Supporting Information, NbO_2 is still formed when the atmosphere is switched to argon while the calcination temperature and time are kept identical (900°C for 4 h). These results suggest that the hydrogen gas is not crucial for the reduction of Nb_2O_5 to NbO_2. Furthermore, when the calcination temperature is lowered down from 900 to 800 °C, only Nb_2O_5 is observed by XRD after calcination under the Ar/H_2 atmosphere for 4 h (Figure S4b, Supporting Information). Thus, the calcination temperature is crucial for the phase transition process, even though low temperature reduction of Nb_2O_5 into NbO_2 has been reported in the literature.[3c] To understand the mechanisms governing the phase transition from Nb_2O_5 to NbO_2, a systematic structure characterization is applied on the niobium oxide/carbon samples prepared with different Bis-GMA/NbETO mass ratios. The porosity evolution along with decreasing Bis-GMA/NbETO mass ratios is investigated by BET measurements (**Figure 3**a and Figure S5, Supporting Information) and SAXS analysis (Figure S6 and Table S2, Supporting Information). Based on the Barret–Joyner–Halenda (BJH) method, the Nb_2O_5/carbon samples (Bis-GMA/NbETO mass ratios of 4:1, 2:1, and 1:1) present average pore sizes of less than 2 nm, indicating a microporous structure. The pore size shifts to 3 nm for the NbO_2/carbon samples prepared with the Bis-GMA/NbETO mass ratios of 1:1.5 and 1:2, referring to a transition to mesoporous structures.[11] Moreover, another pore size of 6.4 nm is presented regarding the NbO_2/carbon nanohybrids. The BET surface areas are also increased from 1.4[1] to around 200 m^2g^{-1}, with increasing NbETO content, which is consistent with the pore size evolution trend (Table S1, Supporting Information). A similar structure evolution is revealed by SAXS (Figure S6, Supporting Information). It is reported that an internal condensation takes place through dehydration between the Bis-GMA polymer chains during the heat treatment, which induces the formation of glassy carbon featured with a low specific surface area (Figure S7a, Supporting Information).[12] The addition of the NbETO precursor suppresses the internal condensation reaction due to the alcoholysis process between NbETO and Bis-GMA molecules (Figure S7b, Supporting Information). Nuclear magnetic resonance (NMR) and FT-IR results confirm the elimination of hydroxyl groups in Bis-GMA after the mixture of two reactants (Figure S8, Supporting Information). With low NbETO contents (Bis-GMA/NbETO mass ratios of 4:1, 2:1, and 1:1), the internal condensation process of Bis-GMA is not significantly interfered by the NbETO species, where a dense carbon matrix with a low specific surface area is still formed after calcination. However, with a Bis-GMA/NbETO mass ratio of 1:1.5 and 1:2, the incorporation of NbETO into the Bis-GMA polymer matrix drastically destroys the internal condensation process by forming coordination bonding with the hydroxyl functional groups within the polymer chains. As a result, the formation of the dense carbon matrix is significantly inhibited and porous structures are generated, as evidenced by the nitrogen adsorption/desorption measurements and SAXS data.[12d]

Based on the comprehensive structure characterization of the niobium oxide/carbon nanohybrids prepared with systematically tuned Bis-GMA/NbETO mass ratios, the mechanism for the formation of NbO_2 is proposed (Figure 3c). The major experimental results of the phase transition of the niobium oxide can be summarized as follows:

1) The formation of NbO_2 starts with a Bis-GMA/NbETO mass ratio of 1:1.5 and a pure NbO_2 phase is obtained in case of a mass ratio of 1:2.
2) The phase transition is triggered with a calcination temperature above 900 °C, and no phase transition occurs at 800 °C.
3) The phase transition takes place under the calcination atmosphere of either argon or argon/hydrogen mixture.

It is worth pointing out that Nb_2O_5 is not reduced to NbO_2 when the carbon content is high, where the Nb_2O_5 nanoparticles are well embedded in a dense carbon matrix with a very low specific surface area. It is reasonable to speculate that the typical solid–solid-interphase-based carbothermal reduction is unlikely involved. A solid–gas phase reaction mechanism is proposed governing the reduction of the Nb_2O_5 nanoparticles.[13] As shown by the chemical reaction Equations (1-a) and (2-a), the carbon matrix initially reacts with the residual amount of CO_2 in the tube furnace to generate CO.[14] The reduction process is triggered via the reaction between CO and Nb_2O_5. The generated CO_2 further reacts with the carbon matrix to release CO, which reduces Nb_2O_5 to NbO_2 and produces CO_2. According to Equation (1-a), each CO_2 molecule reacting with carbon generates two CO molecules. As a result, the reduction process features a self-amplification, where trace amounts of CO_2 trigger the reduction process and reduce the entire Nb_2O_5 nanoparticles embedded within the carbon matrix. Nevertheless, apart from the existence of CO_2, the porosity and reduction temperature are both crucially influencing the reduction process. With a low specific surface area, the gas penetration into the Nb_2O_5/C nanohybrid to initiate reduction at the solid–gas interface is inhibited and consequently the reduction process is suppressed. As a result, no detectable Nb_2O_5 is reduced to NbO_2 with Bis-GMA/NbETO mass ratios of 1:0, 4:1, 2:1, and 1:1. When the Bis-GMA/NbETO mass ratios reach 1:1.5 and 1:2, a reduction of Nb_2O_5 is observed, which indicates that a high specific area is essential for the phase transition from Nb_2O_5 to NbO_2. Regarding the impact of the reduction temperature, it is found that the reduction process is only possible at

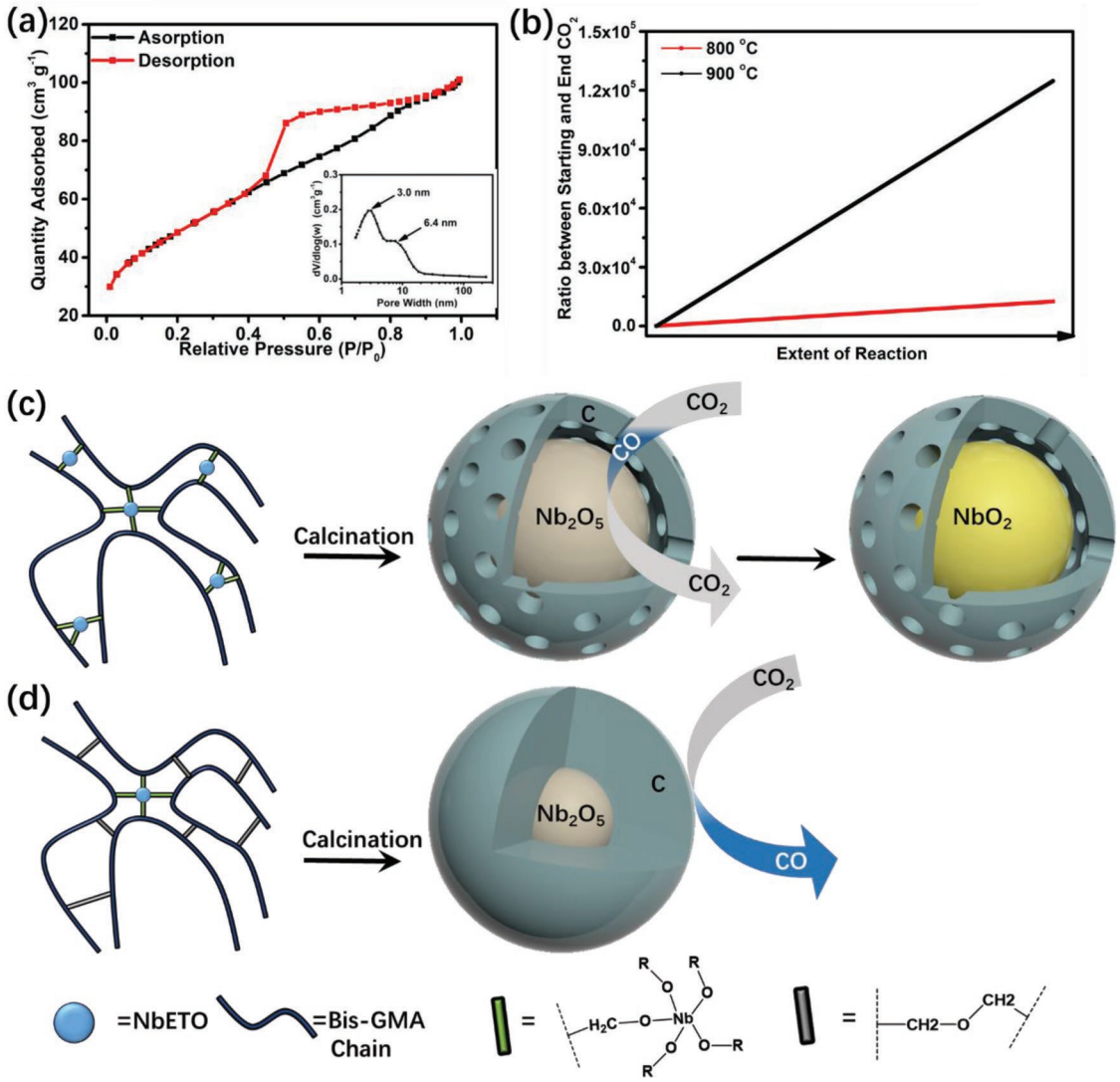

Figure 3. a) N_2 adsorption/desorption isotherms of NbO_2/carbon nanohybrids. Inset a: corresponding BJH pores size distribution curves; b) estimation of CO_2 evolution under 800 and 900 °C; c) schematic illustration of the phase transition for niobium oxide in the niobium oxide/carbon nanohybrids prepared with the Bis-GMA/NbETO mass ratio of 1:2 and d) mass ratios of 4:1, 2:1, and 1:1; light-blue and dark-blue box: alcoholysis site between NbETO and Bis-GMA; light green and dark green box: dehydration site between Bis-GMA.

a temperature higher than 900 °C, while no reduction product is observed with the temperature of 800 °C. However, previous work shows that carbon can react with CO_2 at 800 °C to generate CO.[15] Thus, the reduction reaction between Nb_2O_5 and CO has a temperature threshold. The estimated Gibbs free energy values of the reduction process at 800 and 900 °C are all negative (Equation (2-b)), indicating that the reduction is thermodynamically possible at both temperatures.[16] This suggests that kinetics plays a role in the reduction process. It is reported that the chemical equilibrium constant of Equation (1-a) at 900 °C is 10 times higher than that at 800 °C (800 °C K_p = 7.1, 900°C K_p = 75.4), which makes it possible to estimate the CO_2 content generated by the reaction cycle at different temperatures (Equations (1-a) and (2-a)).[17] Figure 3b shows that the CO_2 amount difference between 900 and 800 °C is increased constantly along with increased reaction extent. As a result, the reduction extent is significantly enhanced if the temperature is increased from 800 to 900 °C, leading to a full phase transition from Nb_2O_5 to NbO_2

$$CO_2 + C \rightarrow 2CO \quad (1\text{-a})$$

$$\Delta G = -38\ \text{kJ mol}^{-1}\ 1200\ \text{K} \quad (1\text{-b})$$

$$Nb_2O_5 + CO \rightarrow 2NbO_2 + CO_2 \quad (2\text{-a})$$

$$\Delta G = -351.9\ \text{kJ mol}^{-1}\ 1200\ \text{K} \quad (2\text{-b})$$

2.2. Electrochemical Performance of NbO_2/Carbon Nanohybrids

The electrochemical performance of the NbO_2/carbon nanohybrids is investigated as coin type half-cells. **Figure 4**a displays

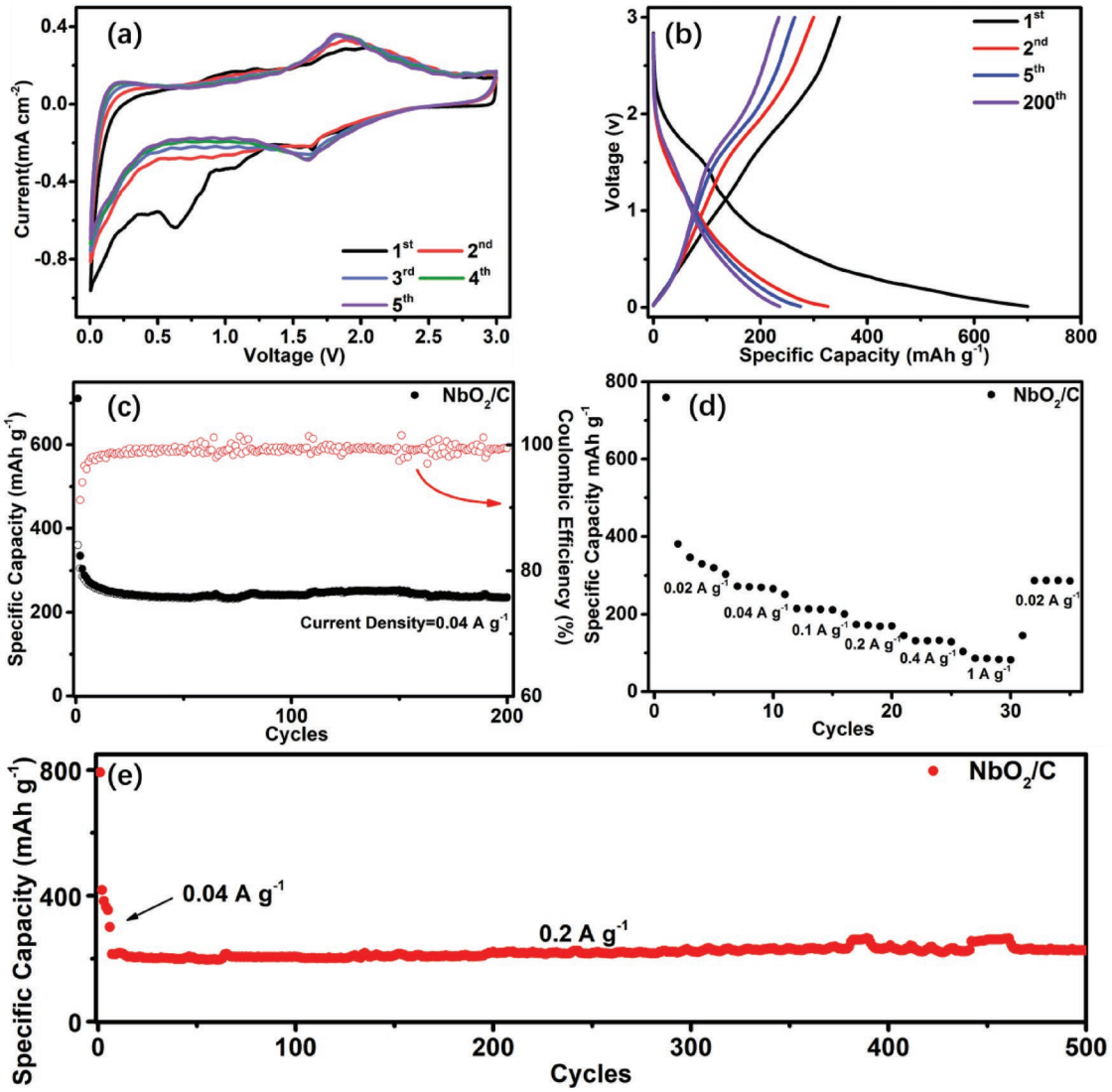

Figure 4. Electrochemical performance of the NbO_2/carbon nanohybrids. a) CV curves, b) charge–discharge profiles, c) cycling performances at 0.04 A g^{-1}, d) rate performances, and e) long cycling performances at 0.2 A g^{-1}.

the cyclic voltammetry (CV) curves of the NbO_2/carbon nanohybrids at a scanning rate of 0.2 mV s^{-1} and in a voltage window of 0.001–3 V. A reductive peak at 1.5–1.75 V and two broad oxidative peaks at 1.0–1.2 V/1.8 V are observed in the CV profiles, which are assigned to the delithiation/lithiation processes of NbO_2. Besides, a broad reductive peak appears at 1.2 V in the initial cycle, referring to the formation of a solid electrolyte interphase (SEI) from the carbon matrix.[18] Small peaks at around 0.5 V could be assigned to the lithiation into the resin-derived hard carbon.[19] Furthermore, the carbon component contributes to the lithiation peaks below 1.0 V as well. A similar delithiation/lithiation behavior is seen from the charge/discharge profiles of the NbO_2/carbon nanohybrids with a voltage range of 0.01–3 V at a current density of 40 mAh g^{-1} (Figure 4b). In the first lithiation cycle, a plateau with a sloping voltage profile between 1 and 1.5 V appears, which is ascribed to the formation of the SEI layer. Corresponding with the CV curves, a plateau between 1.5 and 2 V is observed for the NbO_2/carbon samples, which indicates that NbO_2 is involved in the lithiation process.

The cyclic performance of the NbO_2/carbon nanohybrids is evaluated at a current density of 40 mAh g^{-1} as shown in Figure 4c. First charge and discharge capacities are presented as 711 and 360 mAh g^{-1}, referring to a Coulombic efficiency of 50.6%. The irreversible capacity in the first cycle is related to the formation of the SEI, an irreversible lithium storage in mesoporous structures, and possible side reactions between surface functional groups and lithium.[18,20] After the first few cycles, the capacities start to stabilize with the Coulombic efficiency of more than 99.4% because of the homogeneous embedding of the super-small NbO_2 nanoparticles in the continuous carbon matrix, which enhances the structure stability of the electrode. The fluctuations of the cycle curves likely originate from the temperature change of the ambient measurement environment. After 200 cycles, a reversible capacity of

235 mAh g^{-1} is maintained. According to previously reported work, the capacity contribution of the carbon component within the NbO_2/carbon is estimated to be around 40 mAh g^{-1}.[5b] Figure 4d displays the rate performance of the NbO_2/carbon nanohybrids. Reversible capacities of 410, 269, 212, 172, 127, and 82 mAh g^{-1} at current densities of 20, 40, 100, 200, 400, 1000, and 20 mA g^{-1} are delivered, respectively. When the current density is recovered to 0.02 A g^{-1}, a capacity of 279 mAh g^{-1} is still remaining.

In order to further investigate the cyclic stability of NbO_2/carbon nanohybrids, long cycling tests are carried out for the NbO_2/carbon nanohybrids at a current density of 200 mA g^{-1}. As shown in Figure 4e, in order to fully activate the electrodes, a lithiation/delithiation process for five cycles at a low current density of 40 mAh g^{-1} is performed before the long cyclic performance test. A stable reversible capacity of 225 mAh g^{-1} is retained after 500 cycles, where the slight fluctuation is caused by the temperature variation during the long-term tests. It confirms that the NbO_2/carbon nanohybrid exhibits an excellent cyclic performance at a relative high current density, where both the outstanding cyclic stability and good reversible capacity are displayed. The capacity retention after 500 cycles is 74.8% calculated against the capacity of the 5th cycle, which corresponds to an average decay rate of 0.05% per cycle. Figure S9 and Table S3 in the Supporting Information present a capacity comparison of this work and reported NbO_2 based negative electrodes. It is noted that, to best of our knowledge, our work shows the best cyclability and highest retained capacity after cycling. In addition, the NbO_2/carbon nanohybrids deliver higher capacity than $Li_4Ti_5O_{12}$/carbon nanohybrids synthesized with similar method. The excellent cyclic stability originates from the unique structure featured by the NbO_2/carbon nanohybrid, where the in situ formed NbO_2 nanoparticles are homogeneously embedded in the in situ formed carbon matrix. Figure S10 in the Supporting Information indicates that the capacitance process only contributes around 30% of the capacities, which proves that the diffusion-controlled capacities dominate the lithium storage capability. The mechanical stress of each nanoparticle during lithiation is partially mitigated due to super-small size feature of the NbO_2 nanoparticles.[21] The homogeneous embedding of the NbO_2 nanoparticles within the carbon matrix is also helpful to release mechanical stress. Furthermore, the combination of nanoparticles and carbon matrix shortens the lithium diffusion length and improves the charge carrier conductivity simultaneously, leading to an enhanced electrochemical performance at higher current densities.[10b,22] The electrochemical impedance spectroscopy results confirm the improved electric conductivity from the carbon matrix as well (Figure S11, Supporting Information).

2.3. Fundamental Lithiation Mechanism of NbO_2/Carbon

It is well accepted that gassing process takes place during discharge/charge processes of the intercalation negative electrode, which is detrimental for practical applications.[23] However, to our best knowledge, no studies have been reported about the gassing behavior of NbO_2 negative electrodes. In the present work, DEMS measurements are carried out to investigate the gas evolution of NbO_2/carbon electrodes (**Figure 5**a), where commercial lithium titanate (LTO) is adopted as a reference sample (Figure 5b) for the first discharge/charge cycle. C_2H_4 (green lines) and C_2H_6 (blue lines) originate from similar voltage window during the discharge cycle, which are attributed to the reduction of ethylene carbonate (EC) and dimethyl carbonate (DMC).[23b,24] H_2 gas (red lines) is observed for both discharge/charge cycles, due to reduction of trace amount of water.[25] However, the evolution of CO_2 (brown red lines), the typical gassing product of LTO, is not observed during the discharge/charge process of NbO_2. It is reported that the CO_2 evolution arises from a catalytic reduction of EC and DMC by Ti^{3+} during charging process.[23b] The absence of CO_2 suggests that the niobium ions do not exercise catalytic effects to reduce EC and DMC. In addition, the aggregate amount of the generated gas is integrated, referring to 21.5 µmol for NbO_2/carbon and 7.3 µmol for LTO. Note that the relevant capacities of the

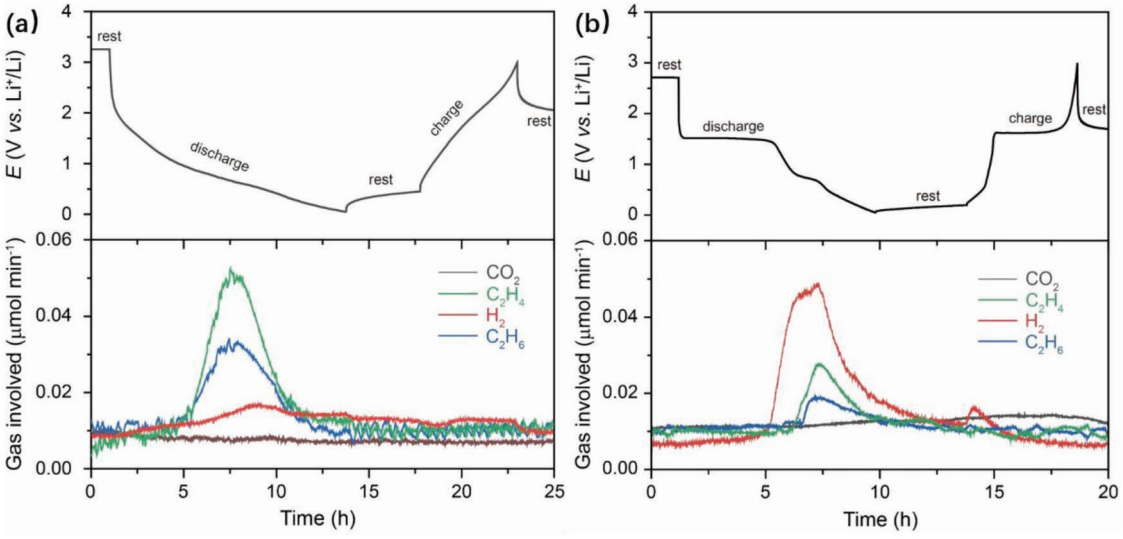

Figure 5. DEMS patterns with initial discharge/charge cycles of a) NbO_2/carbon and b) commercial LTO electrodes.

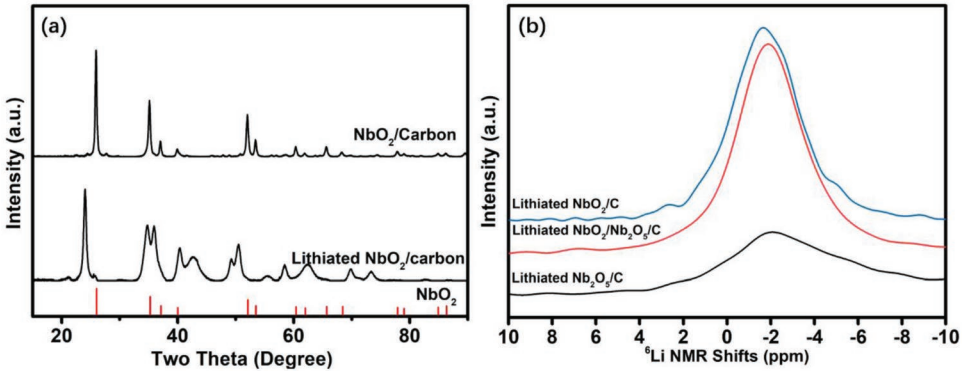

Figure 6. a) Ex situ XRD patterns and b) ^{6}Li MAS spectra of the pristine and lithiated NbO_2/carbon nanohybrids. The NMR spectra are normalized according to the initial mass of the electrodes.

measured cells are 9.0 and 2.4 mAh, respectively, for the NbO_2/carbon and LTO electrodes. Thus, the specific gas amount is 2.39 and 3.00 µmol mAh^{-1}, which indicates that the NbO_2/carbon presents a limited gas process than the commercial LTO.

Ex situ XRD (**Figure 6**a) and ^{6}Li solid-state Magic angle spinning (MAS) NMR (Figure 6b) are carried out on the lithiated NbO_2/carbon nanohybrids to elucidate the lithiation mechanisms. The structures of lithiated Nb_2O_5/C (with Bis-GMA:NbETO feeding ratio of 1:1) and NbO_2/Nb_2O_5/C (with Bis-GMA:NbETO feeding ratio of 1:1.5) are studied by ex situ XRD (Figure S12, Supporting Information) and ^{6}Li solid state MAS NMR as well. ^{6}Li NMR is used instead of ^{7}Li NMR because ^{6}Li has a much smaller quadrupole than ^{7}Li, which leads to a small quadrupolar coupling and paramagnetic interactions with the Nb ions. These interactions tend to significantly broaden the NMR peaks. Therefore, ^{6}Li is adopted to achieve a better spectral resolution.[26] To avoid lithiation of the carbon phase, the samples for ^{6}Li NMR are discharged to 1 V at a current rate of 20 mAh g^{-1}. The lithiated XRD profiles of the three samples both show a small Bragg peak position shift toward smaller two-theta angles as compared to the pristine sample, which indicates the existence of new crystalline phases. In addition, the lithiated NbO_2/Nb_2O/C nanohybrids present two sets of diffraction patterns, corresponding to lithiated Nb_2O_5 and NbO_2, respectively. The numbers and shapes of the XRD profiles of the NbO_2/carbon, Nb_2O_5/carbon and NbO_2/Nb_2O_5/carbon nanohybrids are identical before and after lithiation. It suggests that the lithiation process does not change the crystallographic phases inherited from the pristine counterparts. Based on the XRD analysis, the strong ^{6}Li NMR peaks of the NbO_2/carbon and NbO_2/Nb_2O_5/C nanohybrids located at about −1.6 ppm are assigned to lithiated Li_xNbO_2 (Figure 6b). This suggests that the larger capacities above 1 V of these two samples can be explained by lithiation of Li_xNbO_2. While the corresponding NMR spectra of the Nb_2O_5/C and NbO_2/Nb_2O_5/C show Li sites (broad weak peak around −1.9 ppm), which are assigned to the Li sites in crystalline Nb_2O_5 despite overlapping due to an insufficient resolution.[2e]

The lithium reaction of NbO_2 and Nb_2O_5 could be illustrated as follows[4a]

$$x\mathrm{Li}^+ + x\mathrm{e}^- + \mathrm{NbO_2} \leftrightarrow \mathrm{Li}_x\mathrm{NbO_2} \quad (3)$$

$$x\mathrm{Li}^+ + x\mathrm{e}^- + \mathrm{Nb_2O_5} \leftrightarrow \mathrm{Li}_x\mathrm{Nb_2O_5} \quad (4)$$

From the chemical reaction equation, it can be seen that the lithiation of niobium oxide is featured with an intercalation process, while NbO_2 shows a different lithiation behavior as compared to Nb_2O_5.

To further identify the structure of lithiated Li_xNbO_2, theoretical X-ray diffraction patterns of NbO_2 and Li_xNbO_2 are simulated to compare with the experimentally measured X-ray data. The simulated XRD patterns show a small peak shift and slightly decreased intensities after Li insertion (**Figure 7**a). The main diffraction peaks in the experimental XRD are obviously present in the simulated XRD curves, so that the remaining peaks are assigned to the NbO_2 structure. After lithium intercalation, the lattice parameters are slightly modified (from original a = 13.74 Å, b = 13.74 Å, and c = 6.09 Å to a = 13.76 Å, b = 13.77 Å, and c = 6.09 Å). The calculated volume change based on these lattice parameters is less than 0.36% after lithiation, which is consistent with the results from the ex situ XRD (0.32%) data. The results indicate that the NbO_2 has a smaller volume expansion than both Nb_2O_5 (0.69%) and TiO_2 (4%).[2d,27]

It has been reported that two possible lithium insertion sites are involved in the lithiated of rutile TiO_2, which are center and off-center positions with lithium ion coordinated to different neighboring oxygen atoms.[28] Because of the identical crystallographic phase of rutile TiO_2 and tetragonal NbO_2, similar positions are also considered in the Li–NbO_2 system as described in Figure 7c,d. The Li-insertion into center or off-center positions exhibits similar stabilities with the formation energy of 0.45 eV/Li ion, which is lower than the calculated value (0.70 eV/Li ion) in the Li–TiO_2.[28] Regarding the Li-center structure of Li-NbO_2, Li is located in the pore center from both planes *ab* and *bc*, which is coordinated with six neighboring oxygen atoms to form an octahedron configuration (Figure 7c). The lengths of the newly formed four Li—O bonds in plane range from 2.03 to 2.28 Å, while the two Li—O bonds on vertex are shortened to 1.85 Å. The off-center Li–NbO_2 refers to Li deviates pore center viewed from axis *b* and *c* (Figure 7d), which is coordinated with only four oxygen atoms to form a tetrahedron coordination with four shorter Li—O bonds lengths from 1.85 to 1.93 Å. The simulation results suggest that the lithium ion is inserted into

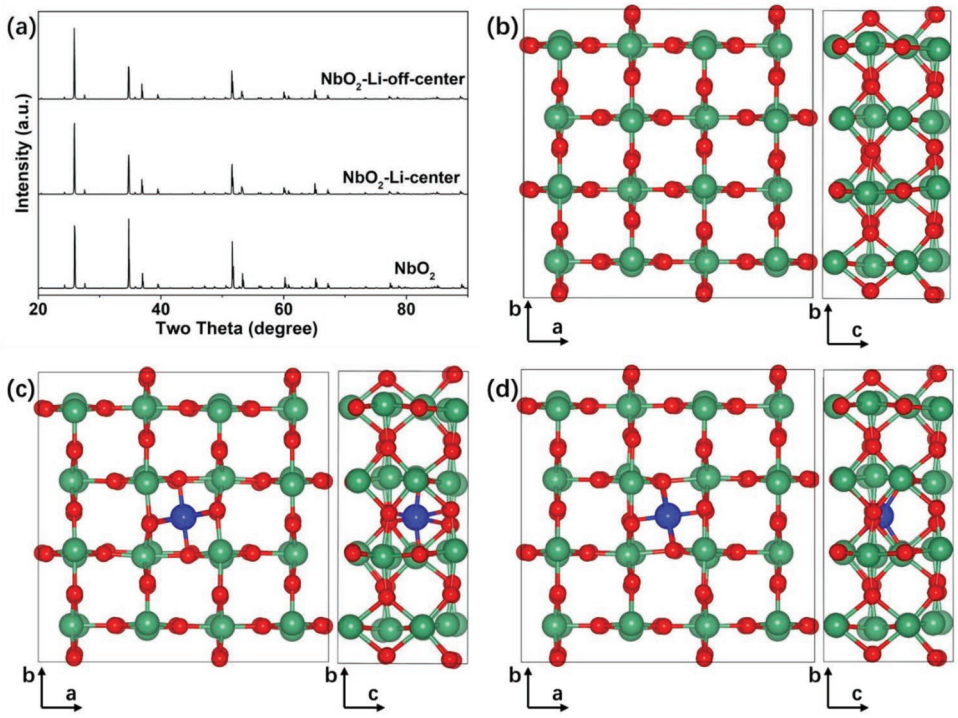

Figure 7. a) Simulated XRD patterns of NbO_2 and lithiated NbO_2. Crystal structure model of b) optimized pristine NbO_2 and Li position at Li–NbO_2 involving c) Li-center and d) Li-off-center positions. All structures are shown from *ab* planes and *bc* planes (lithium: green balls, niobium: blue balls, and oxygen: red balls).

the pore center position from both planes of *ab* and *bc* of the tetragonal NbO_2 (Figure 7b).

3. Conclusions

In summary, NbO_2/carbon nanohybrids are successfully synthesized using the dental resin monomer of Bis-GMA as solvent and carbon source and NbETO as the precursor. The alcoholysis reaction between Bis-GMA and NbETO suppresses the formation of low specific surface area glassy carbon, which facilitates the reduction of Nb (V) into Nb (IV) by in situ generated carbon monoxide. Good size control and spatial distribution of the NbO_2 nanoparticles are achieved because of a limited melting process of the cross-linked polymerized Bis-GMA as confirmed by both imaging and scattering techniques. A reversible capacity of 225 mAh g^{-1} remains after 500 cycles at 0.2 A g^{-1} for NbO_2/carbon nanohybrids with Coulombic efficiencies of more than 99.4%. The lithiation mechanism of the NbO_2/carbon nanohybrid is investigated by solid-state NMR, ex situ XRD, DEMS, and density functional theory (DFT) calculations. A low volume expansion (0.3%) upon lithiation and the possible lithium-ion storage site are derived by combing the experimental and simulation results. The DEMS results confirm that the NbO_2 exhibits a limited gas-evolution behavior as compared to commercial LTO negative electrodes. Thus, our work suggests that NbO_2/carbon nanohybrids are promising lithium-ion battery negative electrodes with good reversible capacities, long cycling life, and a limited gassing evolution.

4. Experimental Section

Chemicals: All chemicals were used as received without further purification. NbETO was bought from Alfa Aesar Co., Ltd., UK. Bis-GMA and *tert*-butyl peroxy benzoate (TBPB) were purchased from Sigma-Aldrich. Poly (vinylidene fluoride) (PVDF) was donated by Solvay. Conductive carbon black (Super P) was acquired from SCM Chem. Shanghai, China. *N*-methyl pyrrolidone (NMP) was obtained from Aladdin Reagent Co., Ltd., China.

Sample Preparation: Typical samples were prepared with the following procedures. Bis-GMA and NbETO were mixed with a mass ratio of 1:2 by stirring (≈800 rpm) and heating at around 100 °C until a clear solution was observed. TBPB (2%, mass fraction) was then dropped into the solution mixture as curing agent and homogenized by a Fisherbrand analog vortex mixer at 1500 rpm for 30 s. The as-prepared solution was cured under 150 °C for 2 h. The calcination process was applied on the polymerized samples at 900 °C under argon/hydrogen flow (volume ratio: 95:5) for 4 h in a tube furnace with a ramp rate of 5 °C min^{-1} from room temperature. After calcination, the samples were cooled down to room temperature with the same ramp rate. The calcined NbO_2/carbon nanohybrid powder was then ball-milled in agate jar with a speed of 550 rpm for 30 min (Retsch, PM 100). Control samples with different feeding ratio of Bis-GMA and NbETO were prepared as described in the supporting information.

Material Characterization: The crystallographic phases of the NbO_2/carbon powders were investigated with an X-ray diffraction (XRD; Bruker AXS D8 Advance, $\lambda = 1.5406$ Å, 2.2 kW) in a 2θ range from 5° to 90°. Ex situ XRD patterns of the lithiated electrodes were measured with a Rigaku X-ray diffractometer (9 kW). The morphology of the NbO_2/carbon nanohybrids was characterized by scanning electron microscopy (SEM; Hitachi S4800) and transmission electron microscopy (TEM; Tecnai F20, FEI). Platinum coating was applied before the SEM measurements. The carbon content was determined by thermo-gravimetric analysis (Mettler Toledo) with a temperature range from 50 to 800 °C at a ramp rate of

20 °C min^{-1} in air. Composition of the carbon matrix was characterized by Raman spectroscopy (Renishaw, in Via-reflex). Particle size distribution was determined by dynamic light scattering measurement (Zetasizer Nano ZS; Malvern). The Brunauer–Emmett–Teller (BET) surface area and pore size distribution analysis were carried out by Micromeritics ASAP2020 with N_2 adsorption isotherms at 77 K. Small-angle X-ray scattering (SAXS) measurements were performed using a Ganesha 300XL SAXS–WAXS system (SAXS LAB ApS, Copenhagen/Denmark) with an X-ray wavelength of 1.54 Å and a sample-to-detector distance of 406 mm. Glass capillaries were used as sample containers for the SAXS measurements. X-ray photoelectron spectroscopy measurements were performed with an ESCALAB 250Xi spectrometer, using focused monochromatized Al Kα radiation ($h\nu = 1486.6$ eV) at room temperature. Solid-state nuclear magnetic resonance (NMR) experiments were performed in a 3.2 mm probe-head on a 400 MHz Bruker Advance III spectrometer at the ^{6}Li Larmor frequency of 58.9 MHz. Magic angle spinning (MAS) of 20 kHz was applied. The spectra were recorded with zg30 pulse-acquire sequence (flip angle of $\pi/6$); the $\pi/2$ pulse length was 2.5 µs. The recycle delay was 5 s. The ^{6}Li spectra were referenced by 1.0 M LiCl (aq) at 0.0 ppm.

Electrochemical Measurement: CR 2032-type coin cells were assembled as following to evaluate the electrochemical performance of the NbO_2/carbon nanohybrids. The active materials (NbO_2/carbon nanohybrid powder), super P, and PVDF were mixed with NMP in a mortar with a mass ratio of 8:1:1. The as-prepared slurry was then cast on copper foil and then dried at 80 °C overnight. Electrodes were punched into discs (diameter: 13 mm). Mass loading density of the typical electrode was controlled to be between at 1.5 and 2 mg cm^{-2}. Lithium metal foil (Dongguan Shanshan Battery Materials Co., Ltd.) and Celgard 2400 microporous polypropylene membrane were adopted as counter electrode and separator, respectively. Electrolyte were employed from Zhangjiagang Guotai-Huarong Commercial New Material Co., Ltd., with 1.0 M $LiPF_6$ dissolved in a mixture solution of ethylene carbonate (EC), dimethyl carbonate (DMC), and fluoroethylene (FEC) (EC:DMC:FEC = 1:1:0.5 by volume). Galvanostatic cycling and rate tests were conducted at a voltage range from 0.01 to 3.00 V (vs Li^+/Li) on a Neware Battery Test System. Cyclic voltammetry (0.001–3.00 V, 0.2 mV s^{-1}) and electrochemical impedance spectroscopy (0.001 Hz–1 MHz, 10 mV) measurements were performed on electrochemical workstation (Solartron Analytical.). The lithiated NbO_2/C was prepared through discharging to 0.01 V at a rate of 20 mAh g^{-1}. The electrode was then washed by DMC and dried overnight in a glove box before measurements.

Differential Electrochemical Mass Spectrometry (DEMS) Measurements: DEMS was carried out as described previously.[23b,29] Swagelok cells were assembled with active materials as positive electrode and lithium foil as counter electrode. The generated gas was flushed out from the cell by argon with a flow rate of 0.5 mL min^{-1}. Gas species with molecular weight of 44, 30, 28, and 2 were anticipated to be monitored, referring to CO_2, C_2H_6, C_2H_4 or CO, and H_2.

DFT Calculations: All calculations were based on DFT to optimize geometry structures, which was performed using the Vienna ab initio Simulation Package (VASP).[30] The exchange–correlation interactions of the generalized gradient approximation in the scheme proposed by Perdew–Burke–Ernzerhof functional.[31] The effect of core electrons on the valence electron density was described by the Projector Augmented Wave (PAW) method.[32] The cut-off kinetic energies for the plane waves were set to 500 eV for all calculations. The convergence tolerance of energy and force on each atom during structure relaxation were less than 10^{-4} eV and 0.02 eV $Å^{-1}$. The Brillouin zone was sampled by $3 \times 3 \times 5$ *k*-points using the Monkhorst–Pack scheme for geometry optimization and electronic structural calculations, respectively.[33]

Supporting Information

Supporting Information is available from the Wiley Online Library or from the author. Supporting research data has been deposited in the Oxford Research Archive and is available under this https://doi.org/10.5287/bodleian:JNDdrQ00R.

Acknowledgements

Q.J., Dr. X.G., Dr. Q.Z., and Dr. L.J. contributed equally to this work. The authors would like to thank Prof. Dr. Junliang Sun from Peking University for discussions about XRD data interpretation. This research is funded by the National Key R&D Program of China (Grant No. 2016YFB0100100), the National Natural Science Foundation of China (51702335, 21773279), the Zhejiang Non-profit Technology Applied Research Program (LGG19B010001), Ningbo Municipal Natural Science Foundation (2018A610084), the CAS-EU S&T cooperation partner program (174433KYSB20150013), and Key Laboratory of Bio-based Polymeric Materials of Zhejiang Province. Y.-J. Cheng acknowledges funding by the Marie Sklodowska-Curie Fellowship from EU. S.Y. appreciates the funding support from China Scholarship Council. P.M.-B. acknowledges funding by the International Research Training Group 2022 Alberta/Technical University of Munich International Graduate School for Environmentally Responsible Functional Hybrid Materials (ATUMS). P.G.B. is indebted to the Engineering and Physical Sciences Research Council (EPSRC), including the SUPERGEN Energy Storage Hub (EP/L019469/1), Enabling Next Generation Lithium Batteries (EP/M009521/1), Henry Royce Institute for Advanced Materials (EP/R00661X/1, EP/S019367/1, EP/R010145/1) and the Faraday Institution All-Solid-State Batteries with Li and Na Anodes (FIRG007, FIRG008) for financial support.

Conflict of Interest

The authors declare no conflict of interest.

Keywords

lithium-ion negative electrodes, methacrylate, nanoparticles, niobium dioxide/carbon nanohybrids, thermal polymerization

Received: June 20, 2019
Revised: July 24, 2019
Published online: August 16, 2019

[1] a) M. S. Whittingham, *Science* **1976**, *192*, 1126; b) M. Winter, J. O. Besenhard, M. E. Spahr, P. Novák, *Adv. Mater.* **1998**, *10*, 725; c) M. Reddy, G. Subba Rao, B. Chowdari, *Chem. Rev.* (*Washington, DC, U. S.*) **2013**, *113*, 5364.

[2] a) W. J. H. Borghols, M. Wagemaker, U. Lafont, E. M. Kelder, F. M. Mulder, *J. Am. Chem. Soc.* **2009**, *131*, 17786; b) T. Yuan, Z. Tan, C. Ma, J. Yang, Z.-F. Ma, S. Zheng, *Adv. Energy Mater.* **2017**, *7*, 1601625; c) N. Kumagai, Y. Koishikawa, S. Komaba, N. Koshiba, *J. Electrochem. Soc.* **1999**, *146*, 3203; d) R. Kodama, Y. Terada, I. Nakai, S. Komaba, N. Kumagai, *J. Electrochem. Soc.* **2006**, *153*, A583; e) K. J. Griffith, A. C. Forse, J. M. Griffin, C. P. Grey, *J. Am. Chem. Soc.* **2016**, *138*, 8888; f) Z. Yang, D. Choi, S. Kerisit, K. M. Rosso, D. Wang, J. Zhang, G. Graff, J. Liu, *J. Power Sources* **2009**, *192*, 588; g) J. W. Kim, V. Augustyn, B. Dunn, *Adv. Energy Mater.* **2012**, *2*, 141.

[3] a) Y. H. Cho, S. K. Jeong, Y. S. Kim, *Adv. Mater. Res.* **2015**, *1120–1121*, 115; b) C. S. Kim, Y. H. Cho, K. S. Park, S. K. Jeong, Y. S. Kim, *Key Eng. Mater.* **2017**, *724*, 87; c) H. Park, D. Lee, T. Song, *J. Power Sources* **2019**, *414*, 377.

[4] a) L. Kong, C. Zhang, J. Wang, W. Qiao, L. Ling, D. Long, *Sci. Rep.* **2016**, *6*, 21177; b) H. D. Asfaw, C.-W. Tai, L. Nyholm, K. Edström, *ChemNanoMat* **2017**, *3*, 646.
[5] a) Y. Xiao, X. Wang, Y. Xia, Y. Yao, E. Metwalli, Q. Zhang, R. Liu, B. Qiu, M. Rasool, Z. Liu, J.-Q. Meng, L.-D. Sun, C.-H. Yan, P. Müller-Buschbaum, Y.-J. Cheng, *ACS Appl. Mater. Interfaces* **2014**, *6*, 18461; b) X. Wang, J.-Q. Meng, M. Wang, Y. Xiao, R. Liu, Y. Xia, Y. Yao, E. Metwalli, Q. Zhang, B. Qiu, Z. Liu, J. Pan, L.-D. Sun, C.-H. Yan, P. Müller-Buschbaum, Y.-J. Cheng, *ACS Appl. Mater. Interfaces* **2015**, *7*, 24247; c) L. Zheng, X. Wang, Y. Xia, S. Xia, E. Metwalli, B. Qiu, Q. Ji, S. Yin, S. Xie, K. Fang, S. Liang, M. Wang, X. Zuo, Y. Xiao, Z. Liu, J. Zhu, P. Müller-Buschbaum, Y.-J. Cheng, *ACS Appl. Mater. Interfaces* **2018**, *10*, 2591.
[6] a) X. Wang, J. Q. Meng, M. Wang, Y. Xiao, R. Liu, Y. Xia, Y. Yao, E. Metwalli, Q. Zhang, B. Qiu, Z. Liu, J. Pan, L. D. Sun, C. H. Yan, P. Muller-Buschbaum, Y. J. Cheng, *ACS Appl. Mater. Interfaces* **2015**, *7*, 24247; b) L. Zheng, X. Wang, Y. Xia, S. Xia, E. Metwalli, B. Qiu, Q. Ji, S. Yin, S. Xie, K. Fang, S. Liang, M. Wang, X. Zuo, Y. Xiao, Z. Liu, J. Zhu, P. Muller-Buschbaum, Y. J. Cheng, *ACS Appl. Mater. Interfaces* **2018**, *10*, 2591.
[7] F. Tuinstra, J. L. Koenig, *J. Chem. Phys.* **1970**, *53*, 1126.
[8] Z. Ye, Z. Zhengjun, L. Yuanhua, *J. Phys. D: Appl. Phys.* **2004**, *37*, 3392.
[9] a) M. K. Bahl, *J. Phys. Chem. Solids* **1975**, *36*, 485; b) Z. Weibin, W. Weidong, W. Xueming, C. Xinlu, Y. Dawei, S. Changle, P. Liping, W. Yuying, B. Li, *Surf. Interface Anal.* **2013**, *45*, 1206.
[10] a) Y. Gao, C. Cheng, J. An, H. Liu, D. Zhang, G. Chen, L. Shi, *ChemistrySelect* **2018**, *3*, 348; b) Q. Xu, J.-Y. Li, J.-K. Sun, Y.-X. Yin, L.-J. Wan, Y.-G. Guo, *Adv. Energy Mater.* **2017**, *7*, 1601481; c) M. G. Choi, Y.-G. Lee, S.-W. Song, K. M. Kim, *J. Power Sources* **2010**, *195*, 8289.
[11] K. Zhang, L. Zhang, X. Chen, X. He, X. Wang, S. Dong, P. Han, C. Zhang, S. Wang, L. Gu, G. Cui, *J. Phys. Chem. C* **2013**, *117*, 858.
[12] a) N. Tokiti, I. Michio, *Bull. Chem. Soc. Jpn.* **1964**, *37*, 1534; b) T. Noda, M. Inagaki, S. Yamada, *J. Non-Cryst. Solids* **1969**, *1*, 285; c) G. M. Jenkins, K. Kawamura, *Nature* **1971**, *231*, 175; d) P. J. F. Harris, *Philos. Mag.* **2004**, *84*, 3159.
[13] a) B. V. L'vov, *Thermochim. Acta* **2000**, *360*, 109; b) W. Gruner, S. Stolle, K. Wetzig, *Int. J. Refract. Met. Hard Mater.* **2000**, *18*, 137.
[14] a) S. C. Mitchell, A. Cias, **2004**; b) J. Moon, V. Sahajwalla, *Metall. Mater. Trans. B* **2006**, *37*, 215.
[15] a) J. Fang, B. Gao, A. R. Zimmerman, K. S. Ro, J. Chen, *RSC Adv.* **2016**, *6*, 24906; b) K. Xia, Q. Gao, S. Song, C. Wu, J. Jiang, J. Hu, L. Gao, *Int. J. Hydrogen Energy* **2008**, *33*, 116.
[16] M. Chase, C. Davies, J. Downey, D. Frurip, R. Mcdonald, A. Syverud, *J. Phys. Chem. Ref. Data, Monogr.* **1998**, 9.
[17] Z. L. Min, Shen, *Chem. Ind. Eng. Prog.* **2013**, *32*, 2846.
[18] S. Flandrois, B. Simon, *Carbon* **1999**, *37*, 165.
[19] a) E. Buiel, J. R. Dahn, *Electrochim. Acta* **1999**, *45*, 121; b) H. Fujimoto, K. Tokumitsu, A. Mabuchi, N. Chinnasamy, T. Kasuh, *J. Power Sources* **2010**, *195*, 7452.
[20] a) K. Zaghib, G. Nadeau, K. Kinoshita, *J. Electrochem. Soc.* **2000**, *147*, 2110; b) S.-Z. Liang, X.-Y. Wang, Y.-G. Xia, S.-L. Xia, E. Metwalli, B. Qiu, Q. Ji, S.-S. Yin, S. Xie, K. Fang, L.-Y. Zheng, M.-M. Wang, X.-X. Zuo, R.-J. Li, Z.-P. Liu, J. Zhu, P. Müller-Buschbaum, Y.-J. Cheng, *Acta Metall. Sin. (Engl. Lett.)* **2018**, *31*, 910; c) C. Zhang, L. Gu, N. Kaskhedikar, G. Cui, J. Maier, *ACS Appl. Mater. Interfaces* **2013**, *5*, 12340.
[21] H. Kim, M. Seo, M.-H. Park, J. Cho, *Angew. Chem., Int. Ed.* **2010**, *49*, 2146.
[22] a) S.-H. Ng, J. Wang, D. Wexler, K. Konstantinov, Z.-P. Guo, H.-K. Liu, *Angew. Chem., Int. Ed.* **2006**, *45*, 6896; b) Y. Xu, G. Yin, Y. Ma, P. Zuo, X. Cheng, *J. Mater. Chem.* **2010**, *20*, 3216.
[23] a) M. Lanz, P. Novák, *J. Power Sources* **2001**, *102*, 277; b) M. He, E. Castel, A. Laumann, G. Nuspl, P. Novák, E. J. Berg, *J. Electrochem. Soc.* **2015**, *162*, A870.
[24] a) M. Onuki, S. Kinoshita, Y. Sakata, M. Yanagidate, Y. Otake, M. Ue, M. Deguchi, *J. Electrochem. Soc.* **2008**, *155*, A794; b) Y.-B. He, B. Li, M. Liu, C. Zhang, W. Lv, C. Yang, J. Li, H. Du, B. Zhang, Q.-H. Yang, J.-K. Kim, F. Kang, *Sci. Rep.* **2012**, *2*, 913.
[25] R. Bernhard, S. Meini, H. A. Gasteiger, *J. Electrochem. Soc.* **2014**, *161*, A497.
[26] Y. J. Lee, F. Wang, C. P. Grey, *J. Am. Chem. Soc.* **1998**, *120*, 12601.
[27] M. Wagemaker, G. J. Kearley, A. A. van Well, H. Mutka, F. M. Mulder, *J. Am. Chem. Soc.* **2003**, *125*, 840.
[28] M. V. Koudriachova, N. M. Harrison, S. W. de Leeuw, *Phys. Rev. B* **2002**, *65*, 235423.
[29] a) Y. Chen, S. A. Freunberger, Z. Peng, F. Bardé, P. G. Bruce, *J. Am. Chem. Soc.* **2012**, *134*, 7952; b) X. Gao, Y. Chen, L. Johnson, P. G. Bruce, *Nat. Mater.* **2016**, *15*, 882.
[30] a) S. Grimme, *J. Comput. Chem. Mater.* **2006**, *27*, 1787; b) G. Kresse, J. Furthmuller, *Phys. Rev. B* **1996**, *54*, 11169.
[31] a) J. P. Perdew, K. Burke, M. Ernzerhof, *Phys. Rev. Lett.* **1996**, *77*, 3865; b) J. P. Perdew, Y. Wang, *Phys. Rev. B: Condens. Matter* **1992**, *46*, 12947.
[32] P. E. Blochl, *Phys. Rev. B* **1994**, *50*, 27.
[33] H. J. Monkhorst, J. D. Pack, *Phys. Rev. B* **1976**, *13*, 5.